

LCLS BEAM DIAGNOSTICS*

H. Loos[†], SLAC, Menlo Park, CA 94025, USA

Abstract

An extensive set of beam diagnostics has been one of the factors in the successful commissioning and operation of the Linac Coherent Light Source (LCLS) x-ray FEL over the last seven years. The originally developed and installed diagnostics were geared towards measuring the electron beam parameters of the LCLS design specifications. Since then, a number of improved and new diagnostics has been implemented to accommodate a much wider range of beam parameters and to overcome the challenges of diagnostics for a high brightness electron beam. Plans for the diagnostics of the high repetition rate LCLS-II project and ongoing developments will also be discussed.

INTRODUCTION

The Linac Coherent Light Source (LCLS) free electron laser facility is based on the last km of the existing SLAC linear accelerator using normal conducting copper accelerating structures providing a multi-GeV electron beam at a rate of up to 120 Hz feeding a 100 m long undulator system to generate soft and hard x-rays [1]. The facility has been operating since 2009 delivering up to about 5 mJ photon pulse energy to users during 9 user runs. A comparison of the LCLS baseline performance goals and the presently achieved operational parameters can be found in Table 1.

Over the past years the range of the available electron beam parameters has been significantly widened and new capabilities have been added to the FEL which poses enhanced demands on the existing diagnostics or made the development of new diagnostics necessary. As the baseline LCLS diagnostics has been extensively described in [2, 3], this paper will focus on recent developments. Among them, upgrades to BPM signal processing hardware and RF cavity BPM tests, improvements to the charge measurements, a new wire scanner design to significantly reduce emittance measurement durations and beam tuning time, a beam profile screen less susceptible to coherent radiation effects, and instrumentation to measure the shortest bunches single-shot using coherent radiation detection as well as an X-band deflecting cavity will be presented.

Recently, a new facility, LCLS-II [4], is being planned to enhance the existing LCLS capabilities by providing a MHz rate electron beam from a superconducting accelerator operating at 1.3 GHz feeding two undulator systems to simultaneously generate soft and hard x-ray beams and to generate shorter photon wavelengths using the existing LCLS-I linac, superseding the former LCLS-II

project based on using an existing fraction of the normal-conducting (NC) SLAC 2-mile copper linac. The planned performance parameters can also be found in Table 1 where values in parentheses refer to the Cu-linac.

While the LCLS-II project design benefits from diagnostics improvements already underway, several key parameters of LCLS-II present new challenges to beam diagnostics [5]. The MW beam power greatly limits the use of intercepting diagnostics such as screens and wires which makes it necessary to incorporate low rate diagnostics beam lines into the machine design. Furthermore, the MHz beam rate requires very fast acquisition hardware and software to provide real-time beam pulse synchronized data for machine tuning and fast beam-based feedback systems. Diagnostics developments as they pertain to LCLS-II will be addressed throughout the paper.

BEAM CHARGE MEASUREMENT

The absolute charge measurement at LCLS is designed to be done with a number of toroids distributed at various locations from the injector through the undulator area which then serve as cross-calibration for all the BPM charge measurements. During the initial LCLS commissioning the readings were questionable and an existing toroid still installed from the SLC was used to provide the

Table 1: LCLS and LCLS-II Parameters

	LCLS		LCLS-II
	Baseline	Operation	(Cu)
RF frequency (GHz)	2.856		1.3
Repetition rate (Hz)	120	1 – 120	10 ⁶
Beam energy (GeV)	4.3 – 13.6	2.4 – 15.4	4
Bunch charge (nC)	0.200 & 1	0.02 – 0.25	0.1
Bunch length rms (μm)	20	< 2 – 50	8
Emittance norm. (μm)	1.2	0.13 – 0.5	0.4
X-ray energy (keV)	0.83 – 8.3	0.25 – 10.5	0.2 – 5 (1–25)
X-ray pulse energy (mJ)	< 2	< 4.7	< 2.2
X-ray pulse length (fs)	230	< 5 – 500	60

* Work supported by DOE contract DE-AC02-76SF00515

[†] loos@slac.stanford.edu

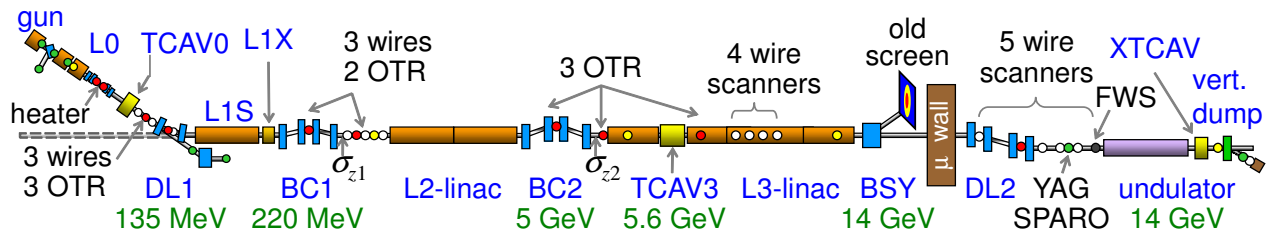


Figure 1: LCLS diagnostics layout. FWS (fast wire scanner), YAG (SwissFEL profile monitor), SPARO (Single-shot bunch length monitor), and XTCAV (X-band transverse deflector) indicate locations of diagnostics discussed in the text.

absolute LCLS bunch charge measurement. Although the toroids had been calibrated using a known test charge, the charge measurements since have shown systematic variations of up to 15% between toroids at the same bunch charge level, and pulse to pulse noise levels of up to 4%, whereas the strip line BPM charge measurement shows typically 0.05% noise at 150 pC. An upgrade project was launched, originally for the normal conduction LCLS-II project, to reach 1% absolute charge accuracy and better than 1% noise to be tested with two toroids in the beam transport line to the undulators. The improved electronics include a 10X amplifier with integrated remote calibrator located in the tunnel at the toroid, differential cables for the up to 500 ft cable run to the service building housing the controls racks, and instead of the previously used Acromag IP330 ADC now a charge ADC, the Caen QDC965A VME module, which is already used for data acquisition of beam loss monitor PMT signals, and which has a 12 bit digitizer with a high and a low signal automatic range selection.

agree to about 1% with each other on the absolute charge and agree to better than 1% to the mean charge reported by the two nearby BPMs. The noise is significantly reduced by about a factor 10 to 0.2–0.5%.

For the LCLS-II charge measurement, one important parameter is the average machine current which will be measured with integrated current transformers like the Bergoz Turbo-ICT, and which will be located in the injector and bunch compressor areas and in each of the beam lines downstream of a beam spreader distributing the beam to the different undulators. A sensitivity down to 1 μ A is required for low charge operation. An independent charge measurement will be provided by a Faraday cup at the end of the low rate diagnostic line in the LCLS-II injector.

BEAM POSITION MEASUREMENT

Several development projects for potential upgrades of the LCLS beam position monitor hardware and analog and digital processing electronics using the μ TCA architecture have been undertaken over the past several years, which were also driven by diagnostics requirements for the former Cu-linac based LCLS-II project.

Stripline Beam Position Monitors

The existing LCLS strip-line BPM receiver electronics [6] was designed to process signals from a single BPM in one crate containing an analog front end (AFE) operating at 140 or 200 MHz with a 7 MHz bandpass filter and 16 bit digitizers. A new BPM receiver and digitizer electronics for strip-line BPMs have been developed in the past years and a test crate has been installed and is operating with first 3 [7] and now 4 BPMs in the L3 linac [8]. The new SLAC built AFE operates at 300 MHz where the strip-line response is higher and has 15 MHz bandwidth. Similar to the previous system, amplifiers and two variable attenuators provide the necessary dynamic range for operation at different bunch charges and a calibration pulse is feed into the strip-lines for self-calibration between beam pulses. A Struck SIS8300 16 bit ADC clocked at 109 MHz is used to sample the signal waveforms. A total of 8 BPMs can be processed in a single 12 slot crate.

The performance of the new system of 3 BPMs is shown in Fig. 3 for a range of 12–350 pC bunch charge. Compared

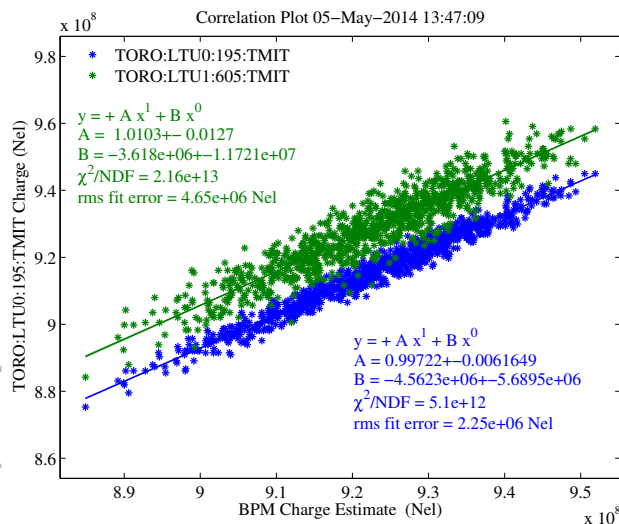


Figure 2: Charge measurement comparison with new toroid electronics and data acquisition. The toroid charge at the two locations is compared to the mean charge measured with two nearby BPMs during an 8 s long duration.

The new system shows the desired performance as can be seen in Fig. 2. The two independently calibrated toroids

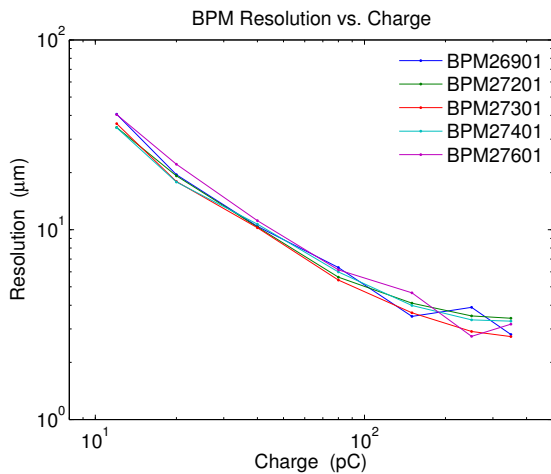


Figure 3: Stripline BPM resolution with new compact μ TCA receiver for bunch charges from 12–350 pC. The first and last BPM 26901 and 27601 equipped with standard LCLS BPM electronics show similar performance.

to neighboring BPMs with a standard receiver the BPMs processed with the new system show almost identical resolution and have been reliably operating for almost 2 years. It remains an open issue that the measured resolution is the same although the processing frequency is better suited to the strip-line length and the bandwidth has been doubled.

Cavity BPMs

In collaboration with Pohang Accelerator Laboratory a new X-band cavity BPM and receiver electronics is being tested in the LCLS undulator beam line adjacent to one of the existing ANL built X-band RF BPMs [9]. The new BPM has been designed and built by PAL [10] and is designed to use 4th harmonic of accelerator frequency at 11.424 GHz compared to standard LCLS undulator cavity BPMs operating at 11.384 GHz to enable arbitrary S-band bucket fill pattern for potential LCLS-I multi-bunch operation. Figure 4 shows the PAL cavity BPM which has the usual monopole reference and dipole cavity but uses coaxial feed-through instead of an RF window and waveguide as implemented for the ANL BPMs.



Figure 4: PAL XFEL RF X-band cavity BPM.

The new down-mix receiver [11] avoids the hydrogen poisoning occurring with the existing RF-BPM receivers which leads to gain deterioration and is designed for low cost using COTS circuits and a wide frequency range 11–13 GHz with only the input filters limiting the bandwidth to 200 MHz. The receiver chassis is located in close proximity to the BPM, and the down-mixed signals are then digitized upstairs of the undulator hall with a μ TCA system similar to the strip-line BPMs using a 4 channel SIS digitizer at 119 MHz. The system schematic is shown in Fig. 5.

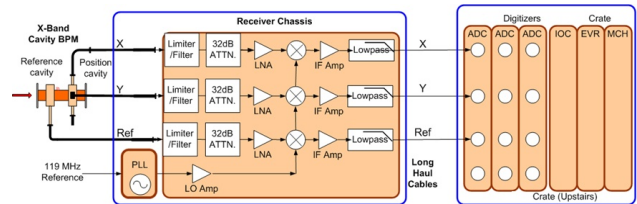


Figure 5: X-band cavity BPM receiver schematic. The μ TCA crate is located outside the undulator hall whereas the receiver chassis is close to the BPM.

Two different cavities installed about 20 cm downstream of the last undulator RF-BPM and supported by the same girder have been tested with beam so far over the last year. The best resolution data achieved is shown in Fig. 6 for the horizontal plane of the first PAL RF-BPM installed with a resolution slightly below 400 nm at 150 pC bunch charge, which is well below the original design goal of 1 μ m for LCLS-II, but is not as good as the resolution of most of the installed ANL RF-BPMs. The elevated noise presently limiting the resolution has since been traced to a bad power supply in the receiver chassis which has been upgraded and beam tests will take place late September at the start of the next LCLS run.

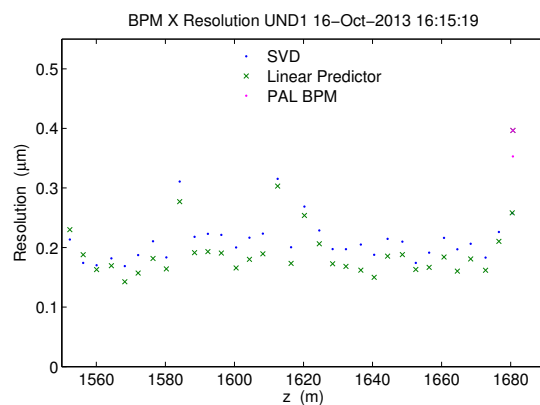


Figure 6: PAL XFEL cavity BPM resolution compared to 33 undulator cavity BPMs measured at 13.4 GeV and 150 pC. The PAL BPM is located at 1680 m and indicated in magenta.

Tests are also underway to use the new receiver with the ANL built BPMs for performance comparison which re-

quires little modification of the receiver to accommodate the different cavity frequency and the waveguide input.

LCLS-II BPMs

The MHz beam rate and the 10 pC low end of the planned charge range pose the main design issues for the LCLS-II accelerator. Strip-line BPMs with about 30 μm resolution at the low charge suffice for most of the normal conducting part of the beam transport. In critical locations where much better resolution is necessary as for energy measurement, fast transverse feedback, beam jitter correction at wire scanners, and undulators, RF cavity BPMs will be installed with X, S, or L-band frequency depending on the measurement function and required beam pipe aperture. Cold button BPMs can be used inside the cryo-modules as a 100 μm resolution is sufficient due to the large aperture of the modules. The high beam rate requires fast processing for several diagnostics and controls elements which will be addressed with the development of a common processing platform [5] including device specific analog front end, fast digitizer, and FPGA data processing, which is then connected to fast timing, machine protection, and fast feedback networks.

BEAM PROFILE MEASUREMENT

Measurements of the transverse size and profile of the electron beam are routinely performed to yield information about the beam's transverse or—via bend magnets and deflecting cavities—longitudinal phase space distribution needed to tune the machine settings to match the design phase space or to optimize beam parameters throughout the accelerator. During the initial LCLS commissioning strong visible coherent effects (COTR) due to the high brightness of the beam were observed on the optical transition radiation (OTR) screens [12] which rendered them insufficient for beam profile measurements at most locations of the accelerator. Several methods of mitigating the COTR effect as well as using and upgrading wire scanners have been explored.

Fast Wire Scanner

As wire scanners are now the predominant transverse profile measurements at LCLS, the originally installed SLC-style scanners suffer from several shortcomings which are being addressed with a new design, based on a linear motor [13]. The SLC-style scanners have a wire card mounted to a shaft which is supported on one end and are driven by a stepper motor. The shaft moves at a 45° angle to the horizontal and has wires oriented horizontally and vertically to sample the respective planes, and a wire at 45° perpendicularly to the scan motion to measure x-y coupling. This setup leads to transverse oscillations of the wire positions up to 10s of μm which could be greatly reduced by implementing either gear reducers or micro-stepping. The achievable speed of less than 1 mm/s means however

that a scan of both transverse profiles at a single wire takes more than a minute and a full emittance measurement requiring scans at four wire locations in the beam line takes several minutes.

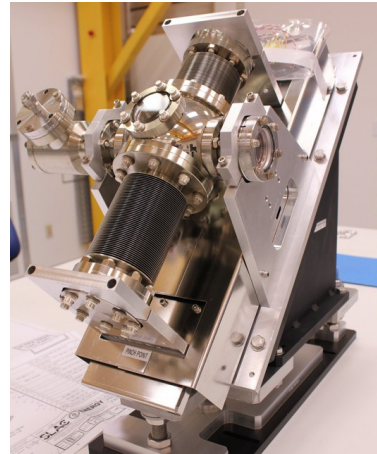


Figure 7: Fast Wire scanner prototype. The beam enters through the right port. Visible are the 45° support stand, the μ -metal shield covering the linear motor, and the two bellows and 6-way cross housing the wire card.

The new fast wire scanner (FWS) design shows in Fig. 7 is normally operated at a maximum speed of 100 mm/s with speeds of 400 mm/s or more being possible by use of a linear motor. It employs a dual bellow design to equalize vacuum forces and to provide a rigid support of the wire card equipped with 3 wires similar to the SLC design. An absolute encoder gives beam synchronous pulse-to-pulse wire position data with sub- μm resolution over the 50 mm actuator stroke. First tests of a FWS installed upstream of the LCLS undulators back-to-back to an existing SLC-style wire scanner show identical beam size measurements, but the scan of both planes takes only a few seconds (see Fig. 8).

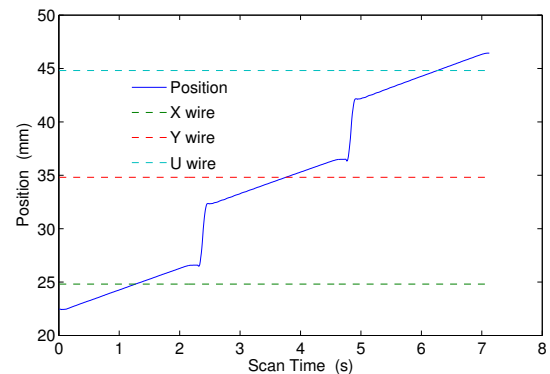


Figure 8: Fast wire scanner motion profile. The solid line shows the encoder read back of the card position, whereas the dashed lines indicate the electron beam intercept position of the respective wire on the card.

At the initial tests of the first fast wire scanner prototype with the electron beam being set up to generate x-rays in the undulators, a drop in the FEL pulse energy was observed, as can be seen in Fig. 9. The drop did not only happen at the point where the carbon wire intercepts the electron beam, but during the entire time when the motor position was away from the initial position. The drop was correlated to orbit oscillations in the undulators of up to $25\ \mu\text{m}$, which is equivalent to the rms electron beam size in the undulators. The orbit kick was originating from the fast wire scanner with magnetic field integral changes of about $20\ \mu\text{Tm}$ depending on the position of the linear motor.

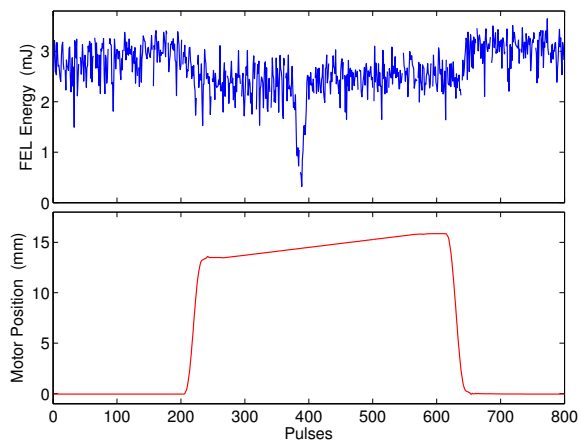


Figure 9: Drop in FEL pulse energy during fast wire scanner prototype scan at 12.4 GeV beam energy. The main dip around pulse number 390 occurs when the electron beam intercepts the carbon wire.

Subsequently, a μ -metal shield was retrofitted to cover the linear motor and the improved version shows field integral changes over most of the scan range below $1\ \mu\text{Tm}$, which is sufficient to guarantee beam steering of less than 10% of the rms beam size at all LCLS wire scanner locations. Plans to replace most of the existing LCLS wire scanners are underway.

A similar design is planned to be used for LCLS-II to enable beam size measurements in the main beam line where the beam repetition rate of up to 1 MHz necessitates much higher scan speeds as the SLC-style scanner provides. A main concern is damage to the wires from the MW beam power. Initial studies of the heat deposition and transport in the wire are based on damage studies of carbon wires in the SLC wire scanners [14]. Figure 10 shows simulations of the relative temperature increase in a $34\ \mu\text{m}$ thick carbon wire during a scan at 240 mm/s wire speed and $40\ \mu\text{m}$ beam size at 0.6 MHz beam repetition rate for various values of thermal diffusivity found in the literature for carbon wires. The final temperature increase in the case of no cooling is due to the heat deposited from the integrated charge density impinging on the wire during the scan, which was chosen to be equivalent to the charge density where no damage

occurred according to [14]. Due to the 45° geometry the actual motor speed needs to be larger than 340 mm/s which has been demonstrated with the present FWS design.

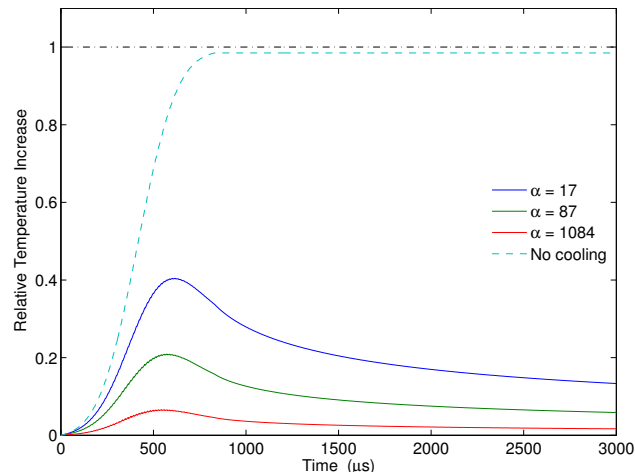


Figure 10: Simulation of carbon wire temperature increase during wire scan. The increase is normalized to the final temperature at the end of the scan assuming no cooling. The thermal diffusivity α is given in mm^2/s .

OTR and YAG Screens

During the initial LCLS commissioning, the OTR screens downstream of the bunch compressors were deemed unusable due to the observed COTR effect [12], but the screens in the injector prior to any bend magnets remained useful as the OTR intensity response was linear with charge. After the installation of the laser heater and its chicane magnets [15] the COTR effect was considered tolerable due to the small R_{56} of 8 mm of the chicane. Recent investigations [16] comparing wire scanner and OTR screen measurement show that the emittance measured with the injector OTR screen agrees well with the wire scanner measurement if the chicane is off. If it is turned on with the heater laser still blocked the emittance is however underestimated by 30%.

Figure 11 shows typical OTR spectra at 135 MeV and 150 pC taken with a transmissive grating placed in front of the lens of the OTR CCD camera. It shows a smooth incoherent OTR spectrum with the chicane off, and a factor 2 higher light intensity with the chicane on, but the heater laser blocked. The COTR effect is much reduced when the heater laser is enabled by adding uncorrelated energy spread to the beam and reducing the micro-bunching instability. The temporal modulation of the electron beam at 766 nm in the laser heater undulator by the laser also causes a modulation at the second harmonic at 383 nm which can be seen in the figure. In both cases when the chicane on on the additional light is emitted preferably in the core of the beam, hence underestimating the true beam size. Emittance measurements for normal beam tuning which requires the laser heater chicane to be on have been regularly done with

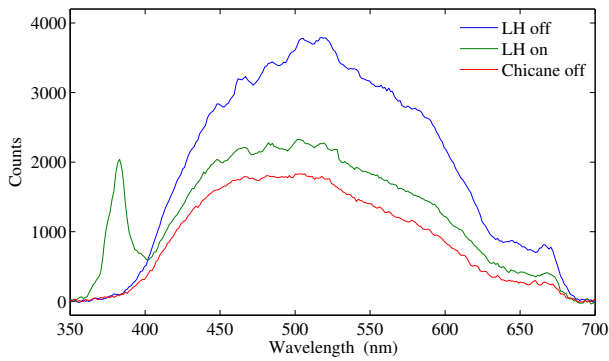


Figure 11: Injector OTR light spectrum for different laser heater (LH) configurations at 150 pC charge. LH on is the normal LCLS operating mode, LH off has the laser beam of the heater blocked, and chicane off also has the chicane bend magnets turned off.

the heater laser blocked as the additional light at the second harmonic was affecting the beam size measurements. Although a suitable optical filter could narrow the spectrum collected by the camera to the central part where the intensity with the laser heater on is only enhanced by about 25%, such a measurement resulted in the beam emittance still underestimated by 30%. The standard injector emittance measurement has now been done for the last year with the adjacent wire scanner. A proper 2-D single shot screen setup needed for reliable time resolved emittance measurements in the LCLS injector remains an open issue as YAG:Ce scintillators saturate at the small beam sizes there [2], but crystals with lower scintillation yield might offer a possible solution.

One method to avoid coherent visible radiation to affect beam profile measurements is to use a screen of a fluorescent crystal rather than an OTR screen, and to have a non-specular viewing geometry so that transition radiation emerging from the crystal surface at a specular reflection angle with respect to the electron beam axis does not enter the camera. Such a screen with various upgrades has been installed for several years in the LCLS main dump line replacing an OTR screen where the YAG crystal is tilted by 7° to the electron beam axis, thus effectively reflecting upstream coherent light away from the camera.

A beam profile monitor with a new fluorescent screen observation geometry developed at the Paul Scherrer Institut (PSI) is now being tested at LCLS [17] at GeV beam energies in a location upstream of the undulators (see Fig. 1). This location was chosen because an OTR screen at approximately the same location had shown in the past the strongest COTR effect with up to 5 orders of magnitude enhancement due to strong bunching at visible wavelengths from the micro-bunching instability. Furthermore, the location enables to measure final slice emittance and bunch length just before the beam enters the undulators by using the deflecting cavity in the main linac.

ISBN 978-3-95450-141-0

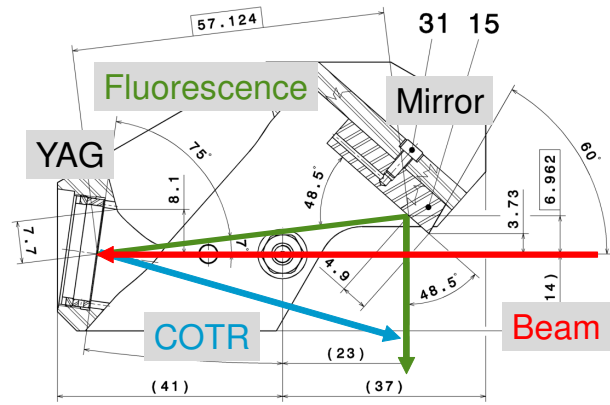


Figure 12: Schematic of the SwissFEL YAG screen.

In the new design shown in Fig. 12, the YAG crystal normal is tilted by 8° to the electron beam axis and the viewing angle of 7° is chosen for optimal resolution so that the line of sight from the camera is in line with the line of fluorescence emitted where the electron beam passes through the crystal, taking refraction at the crystal surface into account. The tilted object geometry is accounted for by tilting the CCD with respect to the lens according to the Scheimpflug principle so that the entire crystal plane can be in focus.

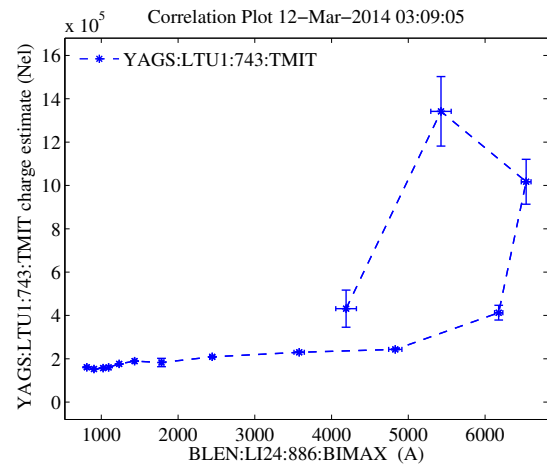


Figure 13: Total CCD counts from SwissFEL YAG screen for different bunch compressions at 160 pC.

The YAG crystal thickness plays a crucial factor in the operation of the profile monitor as the crystal initially installed was 100 μm thick and due to the resulting beam loss the machine protection system only allowed 0.5 Hz operation. The presently installed 30 μm thick crystal now enables 10 Hz beam rate with the beam parked on the tune-up dump before the undulators. Beam sizes as small as 45 μm could be observed to date. Studies of the COTR effect have been made by observing the beam spot brightness while varying the bunch compression (see Fig. 13) which show at full compression a small coherent enhancement of 10–15% for a 20 pC bunch charge at both 4 and 13 GeV.

This is reduced to 5% with the laser heater on. Furthermore, at this low charge no fluorescence saturation effect is observable. At 160 pC coherent effects are more pronounced; with the laser heater off a 10 times enhancement is observed which reduces to factor 2.5 with the laser heater enabled. A slight saturation of the fluorescence at 180 pC could be inferred from a 10% drop in light emission during a scan of an upstream quadrupole. Recently, a yellow filter was installed to narrow the observed spectral range to the green YAG fluorescence to block potential coherent radiation at longer visible wavelengths and first tests indicate considerably less coherent enhancement. Further details of the studies done so far of the profile monitor can be found in [17].

As this design has proven to reduce the COTR effect from many orders of magnitude to a percent effect, it is now being considered for the LCLS-II diagnostics as beam profile monitors in the low energy diagnostics line and for use at low beam rate in the main accelerator beam line and the transport lines to the two undulators.

Overlap Diagnostics

A combination device of a wire scanner and a fluorescent YAG screen is being used for the soft x-ray self-seeding experiment (SXRSS) [18] where after 8 undulators a four dipole chicane separates the electron beam from the x-ray beam, and a setup of a grating and three mirrors acts as a monochromator for the x-rays. A special diagnostics was needed which simultaneously can measure the transverse position of both the electron beam and the x-ray beam at two different locations downstream of the chicane/monochromator setup, so that both beams which are diverted from their straight trajectories can be steered back onto the same axis to enable further FEL amplification in the downstream undulators. As only a YAG screen can sufficiently measure the position of the x-rays of at this point only a few nJ pulse energy, but radiation protection for the undulators prohibits the use of such a crystal for electron beam diagnostics, the beam overlap diagnostic (BOD) device shown in Fig. 14 has been developed which combines a 20 μm thick 10 mm square YAG crystal and two crossed 40 μm thick carbon wires. With an electron beam size of 30 μm rms in the undulators and an x-ray spot size as small as 30 μm an overlap precision of the same value is needed.

In normal beam operation the device is retracted and both beams pass through the cut-out in the left part. A stepper motor with sub-μm encoder resolution and 1 μm position repeatability provides horizontal motion and when inserted, the nominal electron beam axis is indicated by the cross-hair between the vertical wire and the YAG crystal to the right, leaving 1.5 mm clearance of the electron beam to the crystal. The whole card assembly can be viewed with a CCD camera having about 10 μm pixel resolution via a fixed 45° annular mirror in front of the card with a 9 mm hole to provide sufficient stay clear. Two such diagnostics are installed in the inter-spaces upstream of undulators 10

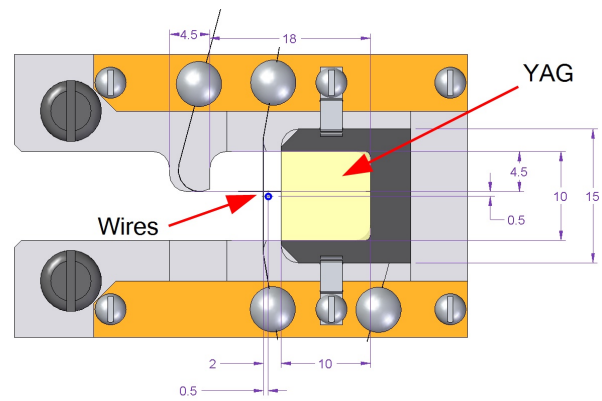


Figure 14: Soft x-ray self-seeding beam overlap diagnostic card. Nominal beam position is at the cross-hair in the center, electron beam position is measured with the adjacent horizontal and vertical wires, and x-ray position with the YAG crystal to the right.

(BOD10) and 13 (BOD13) and supported by the respective girders while the SXRSS setup replaced the undulator located on girder 9.

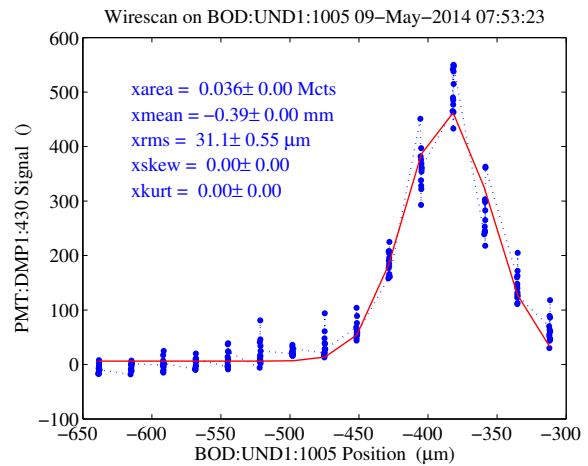


Figure 15: Electron beam position measurement with the BOD.

The electron beam position relative to the wires can be obtained by moving the position of the supporting girder horizontally or vertically, and by recording the electron beam loss signal when the wire is hit, which is shown in Fig. 15. The such established distance between the wires and the electron beam can then be used to determine the pixel coordinates in the camera image of both wires and YAG crystal, and finally to determine the separation between the electron and x-ray beams. The x-ray beam has to be steered away from its nominal position via one of the monochromator mirrors to be visible on the YAG crystal. Once the separation is measured on both screens, the x-ray beam is steered onto the electron beam position using the measured response function of the x-ray mirrors.

Figure 16 shows the camera image of the first overlap

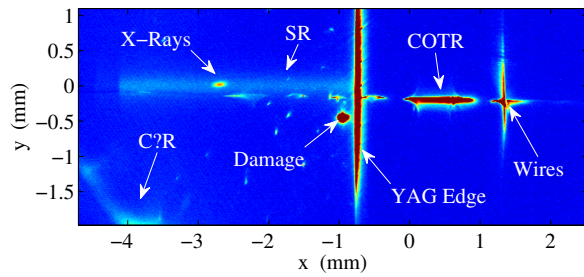


Figure 16: Typical image of the girder 10 BOD diagnostics with the YAG crystal occupying the left and the wires the right part. The annotations indicate the various features visible in the image (see text).

diagnostics. Besides the x-ray spot a number of undesired features are visible which are generated solely by the electron beam. While the synchrotron radiation stripe (SR) is generated from the last bend in the upstream SXRSS chicane and shows steady intensity, the remaining features fluctuate significantly in intensity from shot to shot with up to 100 times the x-ray intensity. The wires can be seen as COTR or coherent optical diffraction radiation (CODR) is generated at the carbon surface where the electron beam is near the wire. The edge of the YAG crystal and a damaged spot are visible by the same mechanism. The radiation labeled “C?R” is however not fully understood. Highly coherent diffraction radiation reflected of the smooth YAG surface would be emitted under small angles to the electron beam and pass through the upstream annular mirror and not be seen by the CCD; however, coherent UV components of this radiation might stimulate fluorescence in the crystal which would be emitted at all angles.

The fluctuating nature of most of the undesired radiation, which is even more pronounced at the second diagnostics, makes it necessary to subtract a background averaged over dozens of images with the x-ray beam blocked. The resulting x-ray to electron beam separation could thus be measured with the required precision to achieve self-seeding [19].

BUNCH LENGTH MEASUREMENT

The generation of shorter and shorter bunches of the high brightness LCLS accelerator in low charge mode to durations of a few fs makes the development of adequate diagnostics necessary as the one originally installed for LCLS was intended for a nominal bunch length not shorter than 20 fs rms. Two such systems have been commissioned during the past year, a single-shot spectrometer (SPARO) and an X-band deflecting cavity, to measure the temporal bunch properties close to the undulators.

ISBN 978-3-95450-141-0

Coherent Radiation Monitor

As coherent radiation spectra based electron bunch length measurements were originally applied to 100s of femtosecond or ps long bunches requiring far-infrared techniques, the few μm rms and shorter bunches at LCLS generate coherent radiation in the near infrared to mid-infrared or even visible spectrum. A single-shot bunch length monitor has been developed at LCLS as a prism spectrometer for the 1–40 μm wavelength range using a KRS-5 prism [20]. As shown in Fig. 17, OTR light from a 1 μm thick Al foil at a location upstream of the undulators is imaged onto a pyroelectric line sensor with 128 elements. The present setup is disruptive to normal beam operation, but could be relocated to non-invasively detect coherent edge or synchrotron radiation from a bend magnet in the upstream beam transport line.

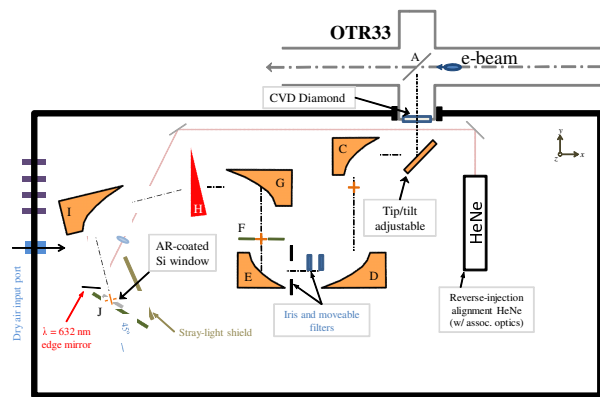


Figure 17: Single-shot mid-IR prism spectrometer.

The use of a prism enables a straightforward coverage of the necessary more than one order of magnitude wavelength range needed for bunch shape reconstruction using a Kramers-Kronig phase retrieval algorithm, however, the resolution is lower than with a grating, and due to the wavelength dependent material dispersion, the resolution and efficiency is also non-uniform and varies considerably over the wavelength range. As the measured spectrum is the product of the bunch form factor of interest with the optical system transmission and spectrometer efficiency, this unknown transfer function needs to be known in order to determine the bunch form factor and eventually the bunch length and temporal distribution. Suitable broadband and calibrated sources are not available to determine the transfer function, so it was found by setting the accelerator to a range of bunch lengths and fitting the measured spectra to a single unknown transfer function and simulated bunch form factors matching the different accelerator settings [20] giving a useful result for wavelengths between 1–20 μm .

Figure 18 shows for four different accelerator bunch compression settings the spectra corrected by the transfer function with extrapolations between 500 cm^{-1} and zero wavenumber where the spectrometer response is too weak, and also the reconstructed bunch profiles at 150 pC and

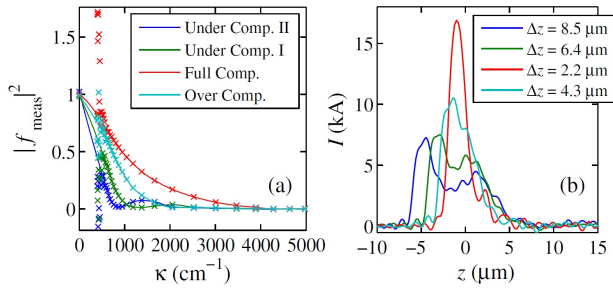


Figure 18: Bunch form factors (a) measured with single-shot prism spectrometer and temporal shape reconstructions (b), adapted from [20].

13.4 GeV. The shortest bunch length is 2.2 μ m FWHM, but at a low charge of 10 pC bunch lengths below 2.2 μ m FWHM could be observed. The 150 pC result is consistent with a 1 μ m rms bunch length measured with the XTCAV (see below) under similar beam conditions. On the long bunch side, lengths of up to 18 μ m FWHM could also be observed.

For LCLS-II the non-interceptive bunch length monitors will also be essential for the fast longitudinal feedback. The average THz radiation power becomes 1000 times higher with otherwise similar beam properties as for the LCLS-I monitors. The single shot bunch length detection necessary at MHz rate becomes a dynamic range issue as attenuating the average power could lower the pulse energy below the noise level. Possible cooling schemes and pyroelectric detector damage thresholds are presently being explored.

Deflecting Cavity

In order to improve the time resolution of the existing S-band deflecting cavity in the L3 linac of about 5 μ m to be able to measure much shorter bunch lengths and resolve finer features in the bunch shape an X-band deflecting cavity was proposed a few years back which would provide a factor 10 or better resolution from the 4 times higher RF frequency and the much higher field gradient possible. Such a cavity was build, installed and finally in 2013 commissioned, and is located downstream of the undulators in the beam line leading to the main beam dump [21]. At this location the diagnostics is non-interfering with FEL user operation as only the spend beam after lasing is affected; it also provides longitudinal phase space informa-

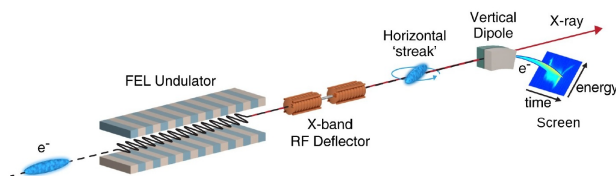


Figure 19: Diagram of the XTCAV diagnostic layout in the undulator dump line, adapted from [21].

tion through the dispersion of the bend magnet by viewing the beam downstream of the magnet via a YAG screen as shown in Fig. 19.

The streaking capacity can be seen in Fig. 20 showing beam sizes at the $\pm 90^\circ$ and XTCAV off setting at 4.2 GeV beam energy and the 20 pC low charge configuration at about half the maximum RF field, where the unstreaked intrinsic beam size corresponds to 1 μ m resolution via the streak or calibration factor of 55 and a bunch length of 1.41 μ m can be obtained. The highest resolution of 1 fs at full RF power has been achieved at soft x-ray beam energies, whereas the resolution at hard x-ray energies is 4 fs.

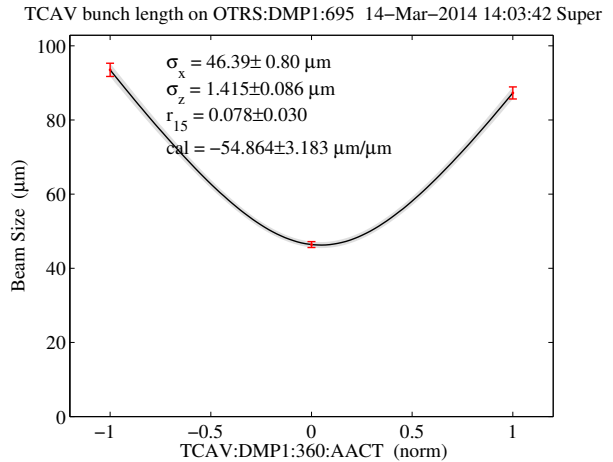


Figure 20: XTCAV bunch length measurement at 4.2 GeV and 20 pC. The three data points for the bunch length fit correspond to settings of -90° , off, and $+90^\circ$.

The main purpose for this development was however the possibility to observe the dynamics of the longitudinal phase space evolution of the electron beam during the lasing process in the undulators as the electrons lose energy due to the interaction with the growing x-rays pulse. The time resolved loss in beam energy is directly proportional to the x-ray power distribution, and the increase in slice energy spread is also related to the x-ray temporal pulse shape. Figure 21 shows a phase space snapshot during soft x-ray beam operation at 4.5 GeV. Details of the x-ray pulse analysis can be found in [21]. These beam images can now be streamed to the x-ray experimental DAQ system to provide offline pulse to pulse x-ray pulse length information. Work is in progress to perform the image analysis in real-time to make this information available at 120 Hz rate [22].

An improved calibration based on absolute measurements with the deflecting cavity in the L3 linac for the relative bunch length monitor after the second bunch compressor [3] which is used in the 120 Hz longitudinal beam based feedback was implemented in Sep. 2013 and could now be cross-checked with the absolute bunch length measurement using the higher resolution XTCAV. The relative error shown in Fig. 22 is only 5% on average over 1 decade of bunch length.

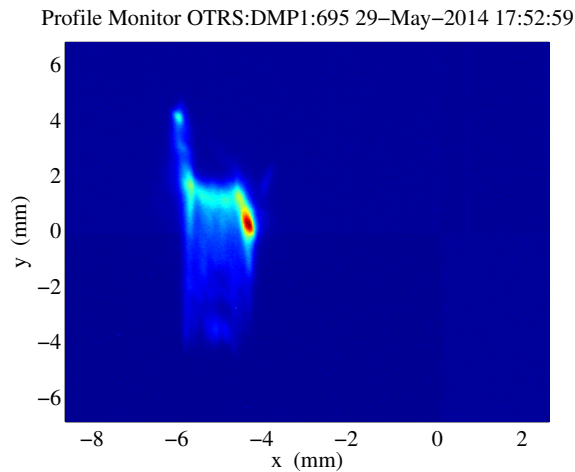


Figure 21: XTCAV measurement of electron beam phase space during soft x-ray self seeding operation. The time is horizontal and the energy vertical. The beam occupying the area below the main brighter part of the beam represents electrons participating in the lasing process.

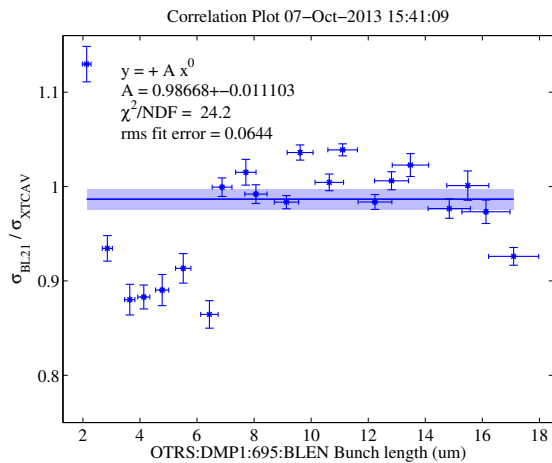


Figure 22: Comparison of post BC2 relative bunch length monitor calibration with XTCAV absolute measurements for 150 pC. The beam energy at the XTCAV was 10.4 GeV.

Besides the x-ray pulse shape determination, the XTCAV has since proven to be an invaluable tool for machine tuning and for many beam physics studies, as the suppression of micro-bunching by the laser heater, or the emittance spoiling of temporal parts of the beam with a slotted foil, or the dynamics of two-bunchlet beam operation can be observed. To further reduce the time resolution, an X-band SLED system as RF pulse compressor is under development, which will double the RF field in the XTCAV and enable 2 fs resolution at hard x-ray beam energies.

ACKNOWLEDGMENT

I wish to acknowledge the many contributions from colleagues at SLAC and collaborators elsewhere to the devel-

opments and results presented here first. For the toroid development I thank Dave Brown, Shantha Condamoor, and Ray Larsen, for the PAL RF BPM collaboration Sandeep Babel, Changbum Kim, Patrick Krejcik, Sonya Hoobler, Andrew Young, and Charlie Xu, and for the fast wire scanner project Scott Anderson, Marc Campell, Antonio Cedillos, Mitch D'Ewart, Patrick Krejcik, Rick Iverson, and Ziga Oven.

REFERENCES

- [1] P. Emma *et al.*, Nature Photonics 4 (2010) 641.
- [2] H. Loos *et al.*, "Operational performance of LCLS beam instrumentation," Proceedings of BIW 2010, Santa Fe, NM, May 2010, p. MOIANB01 (2010).
- [3] H. Loos, "LCLS accelerator operation and measurement of electron beam parameters relevant for the x-ray beam," Proceedings of SPIE, 8778, p. 87780J (2013).
- [4] P. Emma *et al.*, "The linear accelerator design for the LCLS-II FEL facility," Proceedings of FEL 2014, Basel, Switzerland, Aug. 2014, p. THP025 (2014).
- [5] J. Frisch *et al.*, "Electron beam diagnostics and feedback for the LCLS-II," Proceedings of FEL 2014, Basel, Switzerland, Aug. 2014, p. THB04 (2014).
- [6] E. Medvedko *et al.*, "Stripline beam position monitors for LCLS, BIW08, Tahoe City, CA, USA, May 2008, TUPTPF037, p. 285 (2008).
- [7] C. Xu *et al.*, "Design of an ultra-compact stripline BPM receiver using microTCA for LCLS-II at SLAC," Proceedings of IBIC2013, Oxford, UK, WEPC23, p. 731 (2013).
- [8] C. Xu *et al.*, "Commissioning results of MicroTCA.4 stripline BPM system," WEPD17, Proc. IBIC 2014, (2014)
- [9] S. Smith *et al.*, "Commissioning and performance of LCLS cavity BPMs," Proceedings of PAC 2009, Vancouver, BC, May 2009, p. TU3GRC05 (2009).
- [10] H. Choi *et al.*, "About BPMs to be used for PAL-XFEL," Proceedings of IBIC2013, Oxford, UK, MOPC25, p. 112 (2013).
- [11] A. Young, J. Dusatko, S. Hoobler, J. Olsen, T. Straumann, C. Kim, "Performance measurements of the new X-band cavity BPM receiver," Proceedings of IBIC2013, Oxford, UK, WEPC24, p. 735 (2013).
- [12] H. Loos *et al.*, "Observation of coherent optical transition radiation in the LCLS linac," Proceedings of FEL 2008, Gyeongju, Korea, Aug. 2008, p. THBAU01 (2008).
- [13] P. Krejcik, M. Campell, N. Fong, J. Frisch, H. Loos, "Evaluation of new, fast wire scanner designs for the LCLS," BIW 2012, Newport News, VA, April 2012, TUPG035, pp. 210-212 (2012).
- [14] C. Field, D. McCormick, P. Raimondi, M. Ross, "Wire Breakage in SLC Wire Profile Monitors," Proceedings of BIW 1998, Stanford, CA, May 1998, AIP Conf. Proc. 451, pp. 440-445 (1998).
- [15] Z. Huang *et al.*, Phys. Rev. ST Accel. Beams 13 (2010) 020703.

- [16] F. Zhou, K. Bane, Y. Ding, Z. Huang, H. Loos, "Further Understanding of the Linac Coherent Light Source Injector Emittance," Proceedings of FEL 2014, Basel, Switzerland, Aug. 2014, p. THP031 (2014).
- [17] R. Ischebeck, E. Prat, V. Schlott, V. G. Thominet, P. Krejcik, H. Loos, M. Yan, "SwissFEL beam profile monitor," TUCYB3, Proceedings of IBIC 2014, (2014)
- [18] Y. Feng *et al.*, "System design for Self-Seeding the LCLS at Soft X-Ray Energies," Proceedings of FEL 2012, Nara, Japan, Aug. 2012, p. (2012)
- [19] J. Amann *et al.*, "Soft X-ray Self Seeding at the Linac Coherent Light Source," manuscript in preparation.
- [20] T. J. Maxwell, C. Behrens, Y. Ding, A. S. Fisher, J. Frisch, Z. Huang, H. Loos, Phys. Rev. Lett. 111 (2013) 184801.
- [21] C. Behrens *et al.*, Nature Commun. 5 (2014) 3762.
- [22] L. Piccoli, Y. Ding, P. Krejcik, T. J. Maxwell, "Real Time Image Processing for Bunch Length Reconstruction with the XTCAV at the LCLS," MOPD22, Proceedings of IBIC 2014, (2014)